PERGAMON

International Journal of Heat and Mass Transfer 43 (2000) 263–280

International Journal of HEAT and MASS TRANSFER

www.elsevier.com/locate/ijhmt

# Shape of a pore trapped in solid during solidification

P.S. Wei[a,*], Y.K. Kuo[a], S.H. Chiu[a], C.Y. Ho[b]

[a]*Department of Mechanical Engineering, National Sun Yat-Sen University, Kaohsiung 80424, Taiwan, ROC*
[b]*Hwa Hsia College of Technology and Commerce, Taipei, Taiwan, ROC*

Received 17 August 1998; received in revised form 2 April 1999

**Abstract**

The axisymmetric shape of a pore resulting from a bubble trapped by a solidification front is experimentally and theoretically investigated. Accounting for momentum, energy, mass, and species transport and physico-chemical equilibrium at the moving cap surface of the pore and introducing a time-dependent mass transfer coefficient derived from a scale analysis, the results find the effects of dimensionless parameters governing mass transfer coefficient, the maximum and decaying rate of displacement of the solidification front, Henry's constant, concentration in bulk liquid, surface tension, and cap angle on the shape of the pore. Comparisons between the computed and measured variations in the pore length and cap radius with time are also presented. 

## 1. Introduction

The presence of porosities degrades mechanical properties of the workpieces in metals processing such as welding, casting, and crystal growth [1]. Since the solubility of a gas in a solid is much smaller than that in a liquid, the advancing interface rejects gas to liquid and increases concentration near the interface [2–5]. As concentration in the liquid near the interface reaches the gas solubility and satisfies some level of supersaturation, bubbles nucleate, grow and give rise to pores in the solid.

In order to understand the process, water is usually used for a direct observation. The generation and trapping of air bubbles in freezing water have long been well known [6]. For example, distilled water boiled and cooled in air and then frozen contains many pores. Hence, pore-free ice can be produced by directional freezing water boiled in a tube and then sealed to exclude air. Extensive observations were made by Chalmers [7], who interpreted that air rejected by the solidification front accumulates in water near the interface, until concentration is high enough for bubbles to nucleate. The bubble grows because air diffuses into it. If the interface continues to move forward, the bubble cannot grow laterally but forward to form a cylindrical pore, known as an ice worm. The ice worm that frequently looks like a string of pearls was proposed to be due to the fluctuations of the freezing rate. When freezing is slow, the bubbles grow larger. During fast growth, the formation of ice worms is suppressed and the ice contains a large number of very small, round bubbles. Very slow freezing permits the rejected air to diffuse away from the interface, neither bubbles nor ice worms appear. Ice grown in flowing water is usually free of bubbles and ice worms, since the continuous movement of water prevents the build-up of concentration of dissolved air.

Later, Carte [8] found that the density of the separated bubbles in water is related to the solidification rate by a power of $-1.7$. A critical oversaturation for

* Corresponding author. Fax: +886-7-525-4214; +886-7-5254299.

*E-mail address:* pswei@mail.nsysu.edu.tw (P.S. Wei)

0017-9310/00/$ - see front matter 
PII: S0017-9310(99)00134-9

**Nomenclature**

| | |
|---|---|
| $A$, $B$ | dimensionless parameters, defined in Eq. (20) |
| $Bo$ | Bond number $\equiv \rho_l g h_{i0}^2/\sigma_{lv}$ |
| $c_p$ | specific heat |
| $C$ | gas concentration, kg-mole/m$^3$ |
| $C_w$ | gas concentration at cap surface on liquid side, kg-mole/m$^3$ |
| $C_\infty$ | gas concentration in liquid far from bubble, kg-mole/m$^3$ |
| $C_\infty^*$ | dimensionless gas concentration, $C_\infty^* \equiv RTC_\infty/\rho_l g h_{i0}$ |
| $D$ | gas solutal diffusivity, m$^2$/s |
| $g$ | gravitational acceleration |
| $G$ | temperature gradient |
| $h$ | length |
| $h_D$ | mass transfer coefficient, m/s |
| $h_{eff}^*$ | dimensionless parameter governing steady component of mass transfer coefficient, $h_{eff}^* \equiv (h_{i0}/h_g)^{1/2}$, defined in Eq. (16) |
| $h_g$ | effective length of pore |
| $h_0$ | total height of liquid and solid, $h_0^* \equiv h_0/h_{i0}$, as illustrated in Fig. 2 |
| $k$ | conductivity |
| $K$ | modified Henry's constant, $K^* \equiv K/RT$ |
| $L$ | latent heat for solidification |
| $Le$ | Lewis number $\equiv \alpha_l/D$ |
| $m$ | dimensionless parameter governing unsteady component of mass transfer coefficient, defined in Eq. (16) |
| $n$ | mole of gas, kg-mole |
| $p$ | dimensional pressure, $p^* = p/\rho_l g h_{i0}$ |
| $Q$ | dimensionless solid-to-liquid conduction ratio $\equiv k_s G_{s0}/k_l G_{l0}$ |
| $r_i$ | dimensional pore cap radius, $r_i^* = r_i/h_{i0}$, as illustrated in Fig. 2 |
| $R$ | universal gas constant |
| $s_i$ | dimensional displacement of solidification front, $s_i^* = s_i/h_{i0}$, as illustrated in Fig. 2 |
| $S$ | cap area |
| $Ste$ | Stefan number $\equiv c_{pl} G_{l0} h_{i0}/L_{sl}$ |
| $t$ | dimensional time, $t^* = tD/h_{i0}^2$ |
| $T$ | temperature |
| $x_w$ | mole fraction of gas on cap surface and liquid side |
| $z$ | dimensional coordinate, $z^* = z/h_{i0}$, as illustrated in Fig. 2 |

*Greek symbols*

| | |
|---|---|
| $\alpha$ | thermal diffusivity |
| $\rho$ | density |
| $\sigma$ | surface tension |
| $\phi$ | cap angle, as illustrated in Fig. 2 |

*Subscripts*

| | |
|---|---|
| c | cold |
| g | gas in pore |
| h | high |
| i | solid–liquid interface |
| l, s | liquid and solid |
| v | vapor |
| 0 | initial |

*Superscript*

| | |
|---|---|
| * | dimensionless quantity |

bubbles to nucleate is about 30. Wilcox and Kuo [9] reviewed and provided a theory to show that the tendency to form gas bubbles increases with increasing growth rate and ambient pressure and decreasing stirring and height of liquid over solid. Increases in liquid surface temperature either increase or decrease the tendency to nucleate bubbles depending on if the solubility increases or decreases with increasing temperature. Vasconcellos and Beech [10] studied the effects of $CO_2$ dissolved in water on the formation of blowholes. After determining the radius of a blowhole from a photograph, gas pressure and solute concentration were evaluated by applying momentum balance and physico-chemical equilibrium on the bubble, respectively. A blowhole exists when the concentration of solute at the interface proceeds that in equilibrium with gas pressure. The growth of blowholes can be explained in terms of a steady-state solute profile.

Geguzin and Dzyuba [11] observed the bubbles captured by the solidification front in freezing distilled water or naphthalene. Bubbles arose chiefly in the region of coarse distortions of the solidification front at which a local increase in gas concentration exists. The measured density of pores and frequency of the generation of the bubbles increase while the mean sizes of the pores decrease with increasing solidification speed. Geguzin and Dzuba [12] divided bubbles and pores into well-type, semi-closed, closed inclusions, boundary containing gas-saturated liquid, and isolated gas bubble in solid near the solidification front. To evaluate air concentration near the advancing interface a test bubble method was developed. Gas inclusions in

solid were found to be periodic. It was proposed that a bubble is not captured, captured as an elongated inclusion, and isolated pore as the solidification front is, respectively, less, equal, and greater than the rate of displacement of the top surface of the growing bubble. Lipp et al. [13] also applied the test bubble method to study the bubble growth ahead of the solidification front. Tagavi et al. [14] observed void formation in gassed and degassed cyclohexan and 1,4-butanediol solidified from above and below. Blowholes appear for gassed liquids irrespective of the direction of solidification. The freezing process starts with liquid shrinkage and decreasing pressure. In upward solidification, the shrinkage is spread as several voids. Freezing from below causes the void to appear at the top under gravity and at the center under microgravity. The dissolved gases have a tendency to distribute the shrinkage as small worms.

Modeling the growth of a pore resulting from a bubble captured by the moving interface should incorporate with the location and growth rate of the solidification front determined by thermal conditions. It is also difficult to relate the growth of a bubble ahead of the solidification front to the shape of the pore in solid. Recently, Wei et al. [15] observed the formation of the pores in solid and predicted the shape of a pore during upward solidification by accounting for mass, momentum, energy and species transport and physicochemical equilibrium at the moving cap surface. The shape of the pore was found to be strongly affected by solidification rate. Since freezing rate decreases during solidification, mass transfer to the pore and the resulting gas pressure in the pore are reduced. The growth of cap radius is attributed to the decreasing rate of gas pressure overriding that of hydrostatic pressure on the cap surface. As decreasing rates of gas and hydrostatic pressures become the same order in later times, the wall of the pore readily corrugates.

In this study, the work of Wei et al. [15] is extended to investigate the effects of different dimensionless working parameters on the growth and axisymmetric shape of the pore. The mass transfer coefficient governing mass transfer across the cap surface is systematically analyzed from a scale analysis viewpoint. Comparing between the computed and measured results for the growth of the pore leads to a general understanding of the formation of the pores in solid.

## 2. Experimental setup

The main components of the experimental setup are the test liquid, glass tube, constant-temperature bath, and zoom microstereoscope, as illustrated in Fig. 1. A heat-treated glass tube was selected to obtain good thermal insulation. The outer and inner diameters and

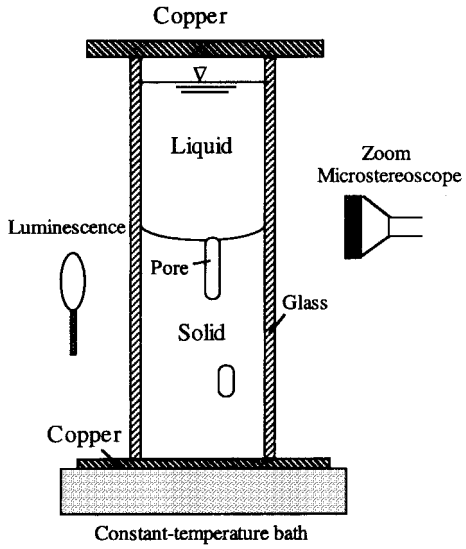


Fig. 1. Schematic sketch of experimental setup.

height are 0.0401, 0.0353 and 0.315 m, respectively. The working medium in the glass tube is distilled water at a height of 0.0975 m. Using other liquids such as a water–KCl solution the nucleated bubbles were too small to be discriminated. The top of the tube is covered by a copper plate to avoid contaminations from the surroundings and maintain a nearly constant atmospheric temperature. The temperature at the bottom can be as low as $-25 \pm 0.3^{\circ}C$ maintained by the constant-temperature bath, where the circulating coolant is 40% volumetric fraction of glycol dissolved in water. The lowest temperature can be changed by varying the amount of glycol. The pipes in the constant-temperature bath are insulated by wool to avoid condensation and freezing of the vapor in the surroundings. Wool is also placed between the compressor and stirring motor to reduce vibration. To reach a long focal distance and clear image, a zoom microstereoscope equipped with a camera is used. The magnification is between 6 to 60. Four light sources are utilized for luminescence. They are cold so that the temperature in water and ice is not disturbed.

## 3. System model and analysis

In this study, solidification is upward in the positive $z$-direction, as illustrated in Fig. 2. The displacement of the solidification front measured from the location where the pore occurs is $s_i$, which is also equal to the length of the pore. The cap radius of the pore is $r_i$ at a depth $h_i$ below the top free surface. The assumptions made are the same as the work presented by Wei et al. [15] and briefly discussed as follows:

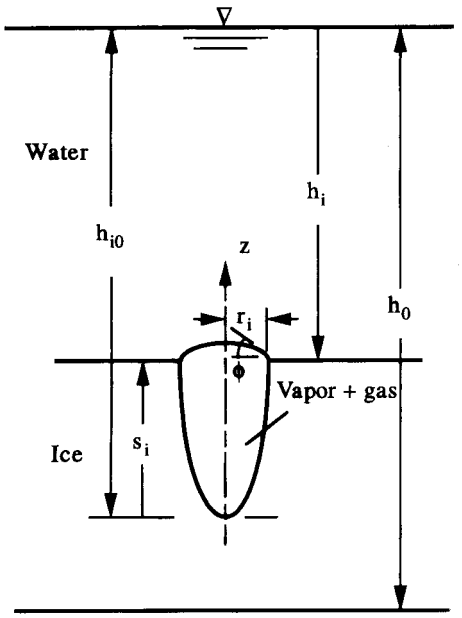


Fig. 2. Physical model and coordinate.

1. The pore is filled with vapor and a gas at the melting point. A gas of multicomponents, however, can be readily extended [9]. The gas and vapor are ideal gases due to low pressure.
2. The growth of the pore is axisymmetric. The cap of the pore is spherical in shape with a constant cap angle.
3. Convection in upward solidification is ignored. The effect of convection due to solidification rate on solute transport is included in the mass transfer coefficient, as can be seen later.
4. Physico-chemical equilibrium on the cap surface of the pore is governed by Henry's law for the solute gas, because dissolved gas in liquid is usually dilute. The measured mole fractions of air, nitrogen, hydrogen, and carbon dioxide gases dissolved in water at 273 K are around $10^{-4}$ to $10^{-5}$ [16–18,25].
5. Mass transfer between cap surface and bulk gas phase is governed by the rate-determining diffusion of the gas in the pore. Bulk resistance of gas is of the order of 100 to 1000 s/m, which is much higher than interfacial resistance of around 0.1 s/m for a water–gas interface without impurities or monolayers [19]. The mass transfer coefficient is time-dependent, since the solute-affected region grows and mass transfer vanishes as solidification rate reduces to zero. Mass transfer on liquid–solid or vapor–solid interfaces is ignored due to negligible solute diffusion and zero convection.
6. All the variables in the pore are lumped as a result of the small size of the pore and long freezing time.

### 3.1. Governing equations

A force balance applied at the cap surface of the pore yields

$$p_g + p_v = p_a + \rho_l g(h_{i0} - s_i) + \frac{2\sigma_{lv}\ \sin\ \phi}{r_i} \tag{1}$$

where the terms on the left-hand-side represent gas pressure in the pore and vapor pressure of the solvent, terms on the right side are atmospheric pressure on the top free surface of liquid, hydrostatic pressure, and pressure due to surface tension, respectively. The partial pressure of the gas is determined by Henry's law [16,17,25]

$$p_g = KC_w \tag{2}$$

where the proportionality constant $K$ is the modified Henry's constant in unit of Pa-m$^3$/kg-mole. Vapor pressure of the solvent, $p_v$, in Eq. (1) can be evaluated from Raoult's law and Clapeyron equation [20]. Since water is a dilute solution pressure of solvent in Eq. (1) is approximately identical to saturation pressure, which is constant at the ice point. Equation of state for the gas in the pore is needed

$$p_g V = n_g RT \tag{3}$$

where the volume of the pore is approximately equal to

$$V = \int_0^t 2\pi r_i(t')[s_i(t) - s_i(t')]\frac{dr_i(t')}{dt'}\,dt' \tag{4}$$

Introducing a mass transfer coefficient $h_D$, the amount of the gas in the pore in Eq. (3) can be evaluated

$$\frac{dn_g}{dt} = h_D S(C_w - C_\infty) \tag{5}$$

The Stefan boundary condition is also required

$$\rho_l L_{sl}\frac{ds_i}{dt} = k_s\frac{dT_s}{dz} - k_l\frac{dT_l}{dz} \tag{6}$$

where the term on the left-hand-side represents latent heat due to solidification while the terms on the right-hand-side are heat conduction from the interface to solid and from liquid to the interface, respectively. The initial condition is $s_i = 0$ at $t = 0$.

### 3.2. Mass transfer coefficient

The mass transfer coefficient in Eq. (5) is defined by conservation of gas solute

$$D\frac{\partial C}{\partial z} \equiv h_D(C_w - C_\infty) \tag{7}$$

where concentration is determined by a species equation in the pore

$$\frac{\partial C}{\partial t} - \frac{\mathrm{d}s_\mathrm{i}}{\mathrm{d}t}\frac{\partial C}{\partial z} = D\frac{\partial^2 C}{\partial z^2} \tag{8}$$

The second term on the left-hand-side of Eq. (8) represents advection with a relative velocity equal to solidification rate in the negative $z$-direction. Scaling Eq. (7) leads to

$$h_\mathrm{D} \sim \frac{D}{\delta_\mathrm{D}} \tag{9}$$

where $\delta_\mathrm{D}$ is the thickness of the solutal boundary layer. Provided that velocity normal to the interface is negligible, Eq. (9) can be represented by

$$h_\mathrm{D} \sim \frac{D}{\delta_\mathrm{eff}} \tag{10}$$

where $\delta_\mathrm{eff}$ is an effective film thickness, as proposed by Lewis and Whitman [21]. In a short period, a balance between unsteady term with solutal diffusion in Eq. (8) leads to

$$\frac{1}{t} \sim \frac{D}{\delta_\mathrm{D}^2} \quad \text{or } \delta_\mathrm{D} \sim \sqrt{Dt} \tag{11}$$

Substituting Eq. (11) into Eq. (9) gives

$$h_\mathrm{D} = \sqrt{\frac{D}{t}} \tag{12}$$

which is the result obtained from the penetration theory of Higbie [22]. If time $t = h_\mathrm{g}/(\mathrm{d}s_\mathrm{i}/\mathrm{d}t)$ where $h_\mathrm{g}$ is an effective length of the pore, Eq. (12) further leads to the representations from Papamantellos et al. [23]

$$h_\mathrm{D} = \sqrt{\frac{D}{h_\mathrm{g}}\frac{\mathrm{d}s_\mathrm{i}}{\mathrm{d}t}} \tag{13}$$

If the process lasts long enough to be in a steady state or involves significant velocity normal to the interface, convection becomes the same magnitude as the diffusion term. Scaling Eq. (8) leads to

$$\frac{\mathrm{d}s_\mathrm{i}}{\mathrm{d}t} \sim \frac{D}{\delta_\mathrm{D}} \quad \text{or } \delta_\mathrm{D} \sim D\left(\frac{\mathrm{d}s_\mathrm{i}}{\mathrm{d}t}\right)^{-1} \tag{14}$$

A substitution of Eq. (14) into Eq. (9) gives

$$h_\mathrm{D} = \frac{\mathrm{d}s_\mathrm{i}}{\mathrm{d}t} \tag{15}$$

which is independent of the solutal diffusion as presented by Davies and Rideal [19]. Combining Eqs. (10), (13) and (15) the mass transfer coefficient can be expressed in a general form

$$h_\mathrm{D} = \frac{D}{h_\mathrm{i0}} h^*_\mathrm{eff}\left(\frac{\mathrm{d}s^*_\mathrm{i}}{\mathrm{d}t^*}\right)^m \tag{16}$$

where the power $m$ is equal to or greater than 0. This indicates that mass transfer is enhanced by the increasing solidification rate. Comparing Eq. (16) with Eq. (13) gives dimensionless parameter governing steady component of the mass transfer coefficient $h^*_\mathrm{eff} = (h_\mathrm{i0}/h_\mathrm{g})^{1/2}$.

### 3.3. Solutions

In view of the Lewis number for a solid and a liquid much greater than unity, temperature profiles in solute-rich regions near the solidification front can be assumed to be linear. Dimensionless temperature gradients in solid and liquid near the solidification front are therefore given by [15]

$$\frac{\mathrm{d}T^*_\mathrm{s}}{\mathrm{d}z^*} \approx 1 - \frac{s^*_\mathrm{i}}{h^*_0 - 1}, \quad \frac{\mathrm{d}T^*_\mathrm{l}}{\mathrm{d}z^*} \approx 1 + s^*_\mathrm{i} \tag{17}$$

Eq. (6) by substituting Eq. (17) yields

$$\frac{1}{Ste\ Le}\frac{\mathrm{d}s^*_\mathrm{i}}{\mathrm{d}t^*} + \left(\frac{Q}{h^*_0 - 1} + 1\right)s^*_\mathrm{i} = Q - 1 \tag{18}$$

Integrating Eq. (18) and introducing the initial condition, as mentioned previously, lead to

$$s^*_\mathrm{i} = A(1 - \mathrm{e}^{-Bt^*}) \tag{19}$$

where dimensionless parameters governing the maximum displacement of the solidification front and exponential decay of displacement are, respectively, defined as

$$A \equiv \frac{(Q-1)(h^*_0 - 1)}{Q + h^*_0 - 1}, \quad B \equiv \left(\frac{Q}{h^*_0 - 1} + 1\right)Ste\ Le \tag{20}$$

Differentiating Eq. (3) with time and substituting Eqs. (2), (4), (5) and (16) leads to [15]

$$p^*_\mathrm{g} = K^* C^*_\infty \left[1 - \frac{K^*}{h^*_\mathrm{eff}}\left(\frac{\mathrm{d}s^*_\mathrm{i}}{\mathrm{d}t^*}\right)^{1-m}\right]^{-1} \tag{21}$$

A dimensionless form of Eq. (1) yields

$$r^*_\mathrm{i} = \frac{2\ \sin\ \phi}{Bo(\,p^*_\mathrm{g} - p^*_\mathrm{a} + p^*_\mathrm{sat} - 1 + s^*_\mathrm{i})} \tag{22}$$

which by differentiating with time gives

$$\frac{\mathrm{d}r^*_\mathrm{i}}{\mathrm{d}t^*} = \frac{-2\ \sin\ \phi}{Bo(\,p^*_\mathrm{g} - p^*_\mathrm{a} + p^*_\mathrm{sat} - 1 + s^*_\mathrm{i})^2}\left(\frac{\mathrm{d}p^*_\mathrm{g}}{\mathrm{d}t^*} + \frac{\mathrm{d}s^*_\mathrm{i}}{\mathrm{d}t^*}\right) \tag{23}$$

Specifying values of independent dimensionless parameters, gas pressure in the pore can be determined

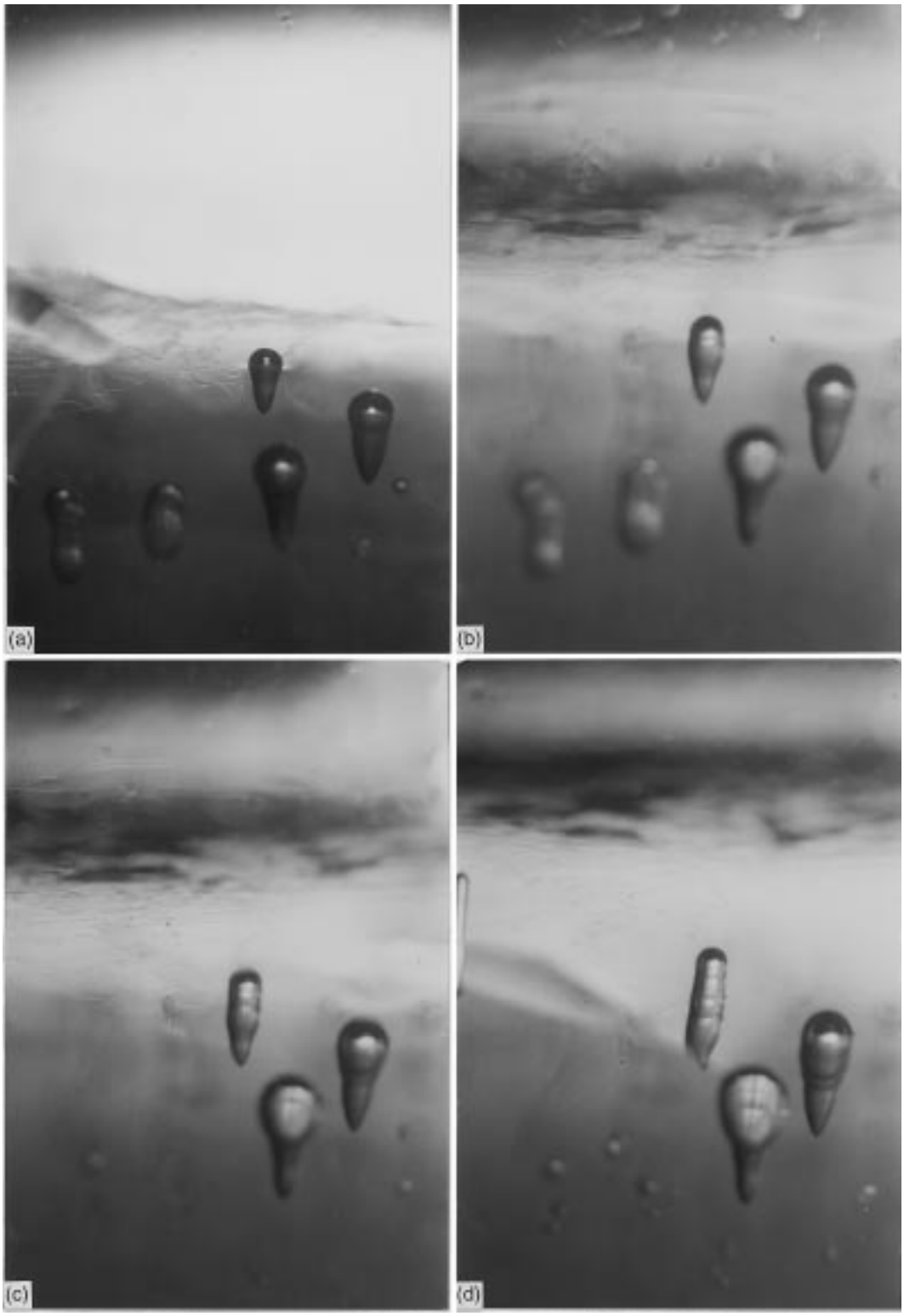


Fig. 3. Photographs with magnification of 20 to describe bubble growth, (a) 0, (b) 5, (c) 20, (d) 50, (e) 130, (f) 190 min.

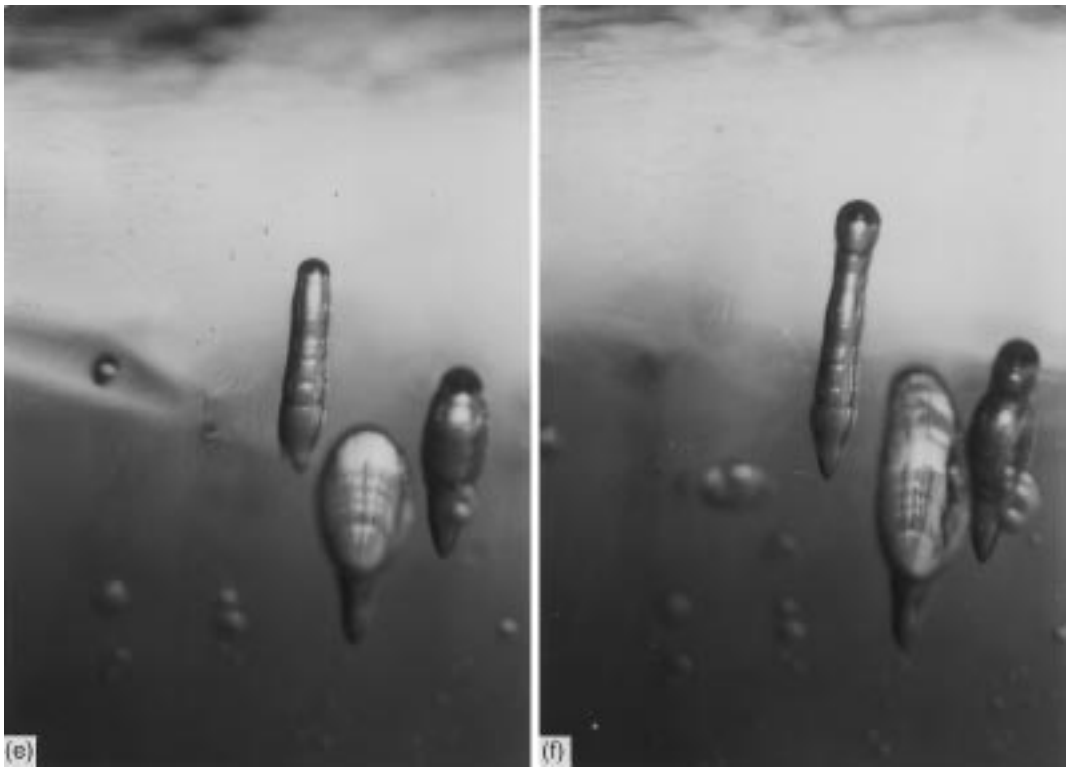


Fig. 3 (*continued*)

from Eq. (21) by substituting Eq. (19). Cap radius is then obtained from Eq. (22).

## 4. Results and discussion

In this study, distilled water is frozen from the bottom of a glass tube at the lowest temperature of $-18 \pm 0.3$°C. The top surface is maintained at a surrounding temperature of 25°C. Observation is provided by Fig. 3(a) showing that several bubbles take place on the solidification front at time $t = 0$. The magnification of the photograph is 20. In view of high gas pressure, the caps of bubbles or pores on the right-hand-side are bulged. The two bubbles on the left-hand-side, however, are slim. Comparing to Fig. 3(a), Fig. 3(b) at a time of 5 min indicates that lengths and radii of bubbles increase with time. The increase in the former is greater than the latter. The increase in the length of a pore is determined by the movement of the solidification front. Interestingly, instead of increasing cap radius, the third bubble from the right-hand-side decreases the radius of the cap. This gives rise to the second ring of streak on the wall of the pore. The third ring on the wall of this bubble can also be seen in Fig. 3(c) at a time of 20 min. The wall of the pore therefore exhibits a periodic nature. It is found that the two bubbles on the left-hand-side disappear due to a low gas pressure resulting in rupture of caps, escape of gases, and entrapment of water. Aside from the fourth streak appears for the third bubble on the right-hand-side, as shown in Figs. 3(d) at a time of 50 min, several small bubbles are found to be nucleated on the lower left-hand-side. Fig. 3(e) shows that the first bubble on the right-hand-side decreases the cap radius at a time of 130 min. The process therefore is repeated for each bubble by referring to Fig. 3(f).

Chalmers [7] proposed that the alternative increase and decrease in cap radius resulted from the fluctuation of the solidification rate. Wei et al. [15] showed that in an earlier stage, cap radius increases with time, even though solidification rate fluctuates. This is because the decreasing rate of the total gas pressure overrides that of hydrostatic pressure (see Eq. (23)). In view of a rapid decrease in gas pressure, the decreasing rate of gas pressure becomes the same order of that of hydrostatic pressure in the later stage of solidification. This results in an oscillation of cap radius.

Different regions of a pore in solid may solidify by examining the second pore from the right-hand-side in Figs. 4(a) and (b) at different times. It shows that the lower region of the pore solidifies owing to an exist-

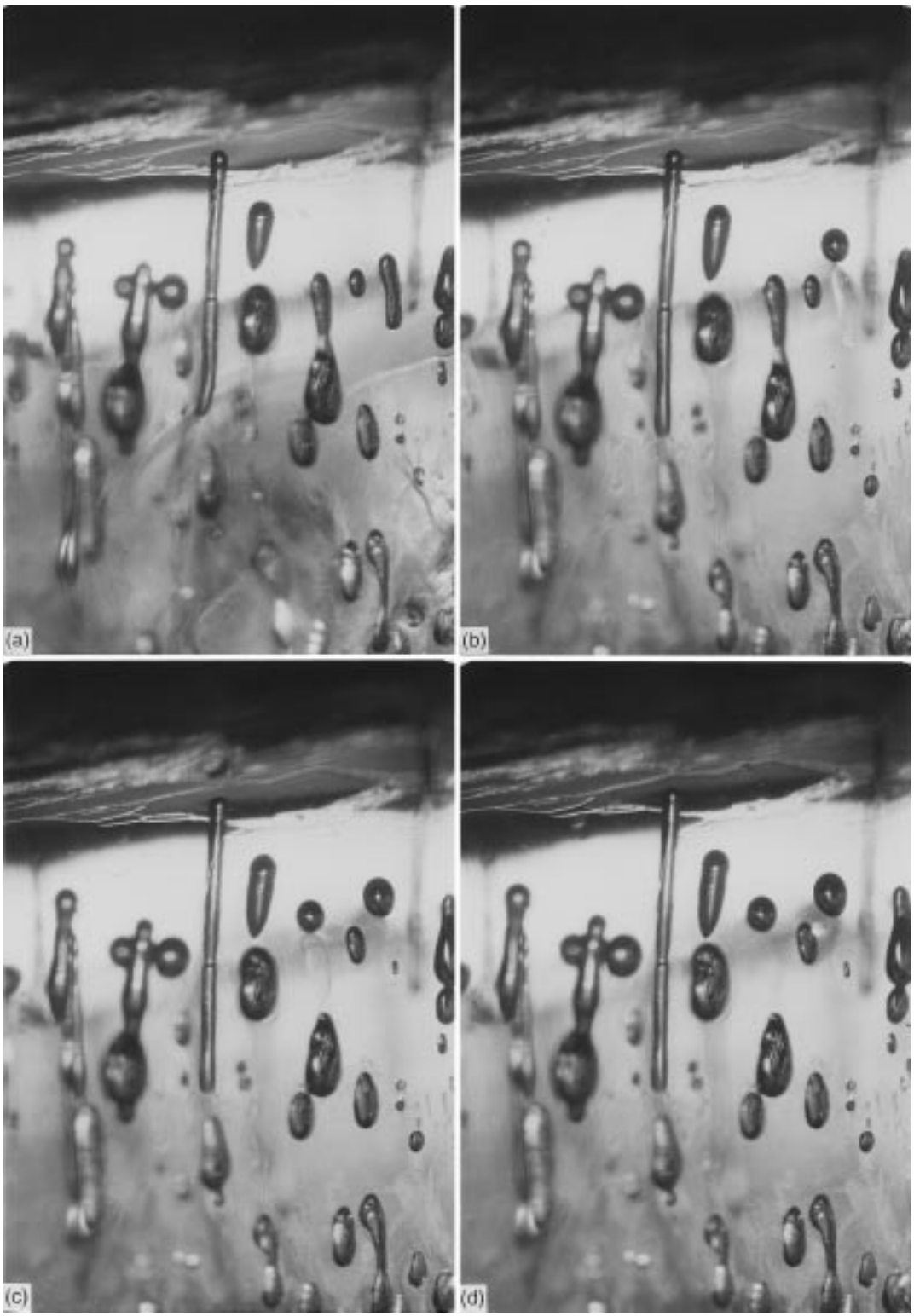


Fig. 4. Photograph showing solidification of pores in a solid during freezing.

Table 1
Typical values of working variables in freezing water

| | |
|---|---|
| $\sigma_{lv}$ (N/m) | 0.076 |
| $k_s$ (W/m-K) | 2.22 |
| $k_l$ (W/m-K) | 0.55 |
| $c_{pl}$ (J/kg-K) | 4205 |
| $\rho_l$ (kg/m$^3$) | 1000 |
| $L_{sl}$ (J/kg) | $3.3 \times 10^5$ |
| $\alpha_l$ (m$^2$/s) | $7.7 \times 10^{-6}$ |
| $p_v$ (Pa) | 611 |
| $K$ (Pa-m$^3$/kg-mole) | $10^7$–$10^8$ |
| $C_\infty$ (kg-mole/m$^3$) | $4.6 \times 10^{-3}$ |
| $D$ (m$^2$/s)[a] | $10^{-5}$ –$10^{-4}$ |
| $G_{10}$ (K/m) | 620 |
| $G_{s0}$ (K/m) | 257 |
| $h_0$ (m) | 0.099 |
| $h_{i0}$ (m) | 0.088 |
| $h_g$ (m) | $4.5 \times 10^{-4}$ |
| $T_h$ (K) | 298 |
| $T_c$ (K) | 255 |

[a] The value of gas diffusivity, $D$, was chosen from Geiger and Poirier [24].

ence of liquid in the pore. The intermediate region of the fourth pore on the right-hand-side also solidifies by comparing Figs. 4(b)–(d).

In this study, dimensionless parameters were estimated from the data suitable for freezing water as presented in Table 1. Fig. 5 shows that dimensionless cap radius and displacement of the solidification front increase while gas pressure decreases as dimensionless time increases. Solidification rate reduces in the course of freezing due to an increase in conduction from liquid to the interface and a reduction of conduction from the interface to solid. At a given time, an increase in dimensionless maximum displacement of the solidification front increases the displacement of the solidification front and solidification rate, which increases gas pressure and decreases cap radius as a result of an enhancement of mass transport. Near the end of solidification dimensionless gas pressure reduces to 120 ($=1.02 \times 10^5$ Pa), which is slightly greater than 1 atm.

The corresponding shapes of the pore in a solid at a dimensionless time of eight are presented in Fig. 6. The shape of the pore at a given time $t$ is determined by the relation between cap radii and the locations of the solidification front from $t = 0$ to $t$. The cap and the base of the pore are not drawn. The base is affected by the nucleation process and is not included in this work. It can be seen that the pore is narrower and longer for a greater dimensionless parameter governing the maximum displacement of the solidification front. Although dimensionless cap radii are close for different values of the dimensionless parameter governing the maximum displacement of the solidification front as dimensionless time increases (see Fig. 5), the shapes of the pore deviate significantly. This is attribu-

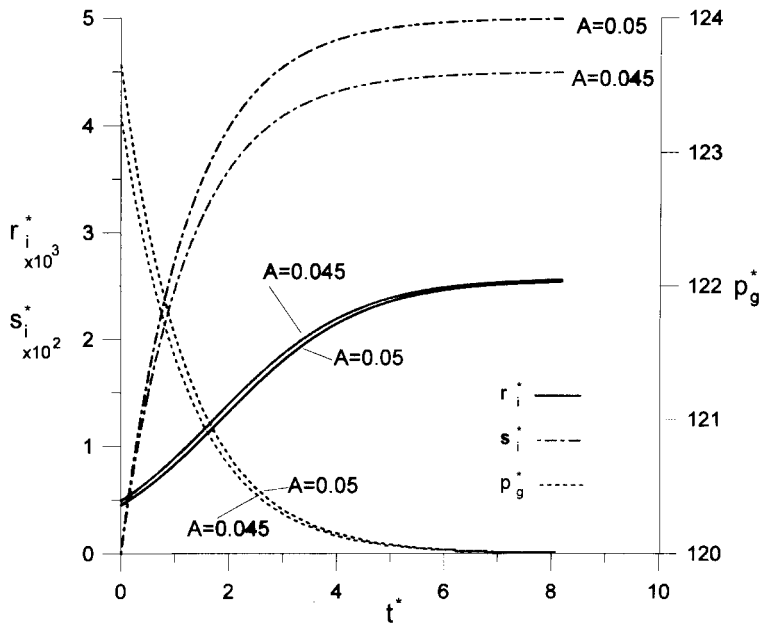


Fig. 5. Dimensionless cap radius, displacement of solidification front, and gas pressure in pore vs dimensionless time for different values of dimensionless maximum displacement of solidification front ($B = 0.8$, $Bo = 10^3$, $m = 0.01$, $K^* = 10$, $C^*_\infty = 12$, $h^*_{eff} = 14$, $\phi = 4\pi/9$).

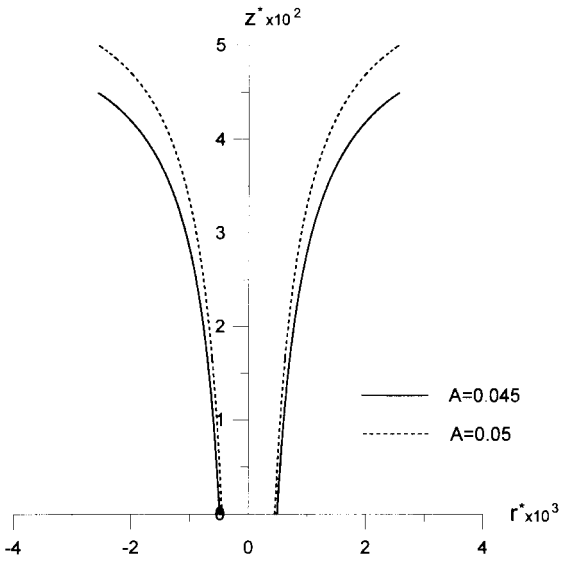


Fig. 6. Shapes of a pore for different values of dimensionless maximum displacement of solidification front ($B = 0.8$, $Bo = 10^3$, $m = 0.01$, $K^* = 10$, $C^*_\infty = 12$, $h^*_{\text{eff}} = 14$, $\phi = 4\pi/9$).

ted to the big difference in the locations of the solidification front.

The variations in the dimensionless displacement of the solidification front, gas pressure, and cap radius with dimensionless time for different values of the dimensionless parameter governing decaying rate of displacement are shown in Fig. 7. As discussed previously, in the earlier stage an increase in the dimensionless parameter governing decaying rate of displacement increases solidification rate, which enhances mass transfer and gas pressure in the pore. As a consequence, dimensionless cap radius reduces. Interestingly, the solidification rate decreases with increasing the dimensionless parameter governing decaying rate of displacement for dimensionless times greater than 1.8. This leads to a reduction of dimensionless gas pressure and an increase of dimensionless cap radius. The axisymmetric shape of the pore in the earlier stage is narrow by increasing the dimensionless parameter governing decaying rate of displacement, as shown in Fig. 8.

Dimensionless gas pressure is reduced and cap radius is increased at a given time by increasing the dimensionless parameter governing the steady component of the mass transfer coefficient, as shown in Fig. 9. An increase in the dimensionless parameter governing steady component of the mass transfer coefficient reduces accumulation of solute at the advancing interface. To satisfy the physico-chemical equilibrium governed by Henry's law, dimensionless gas pressure decreases and cap radius increases. The axisymmetric

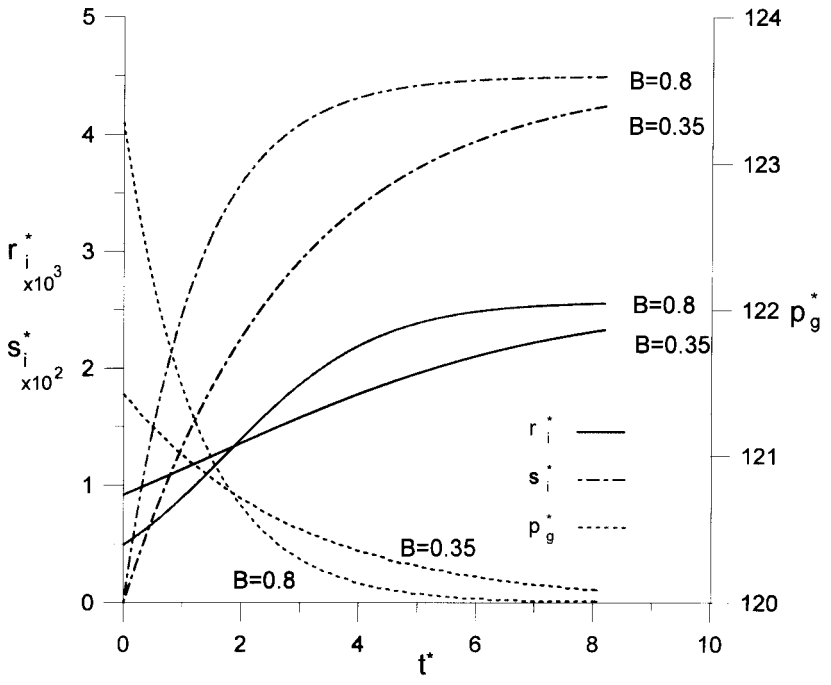


Fig. 7. Dimensionless cap radius, displacement of solidification front, and gas pressure in pore vs dimensionless time for different values of dimensionless parameter governing decaying rate of displacement of solidification front ($A = 0.045$, $Bo = 10^3$, $m = 0.01$, $K^* = 10$, $C^*_\infty = 12$, $h^*_{\text{eff}} = 14$, $\phi = 4\pi/9$).

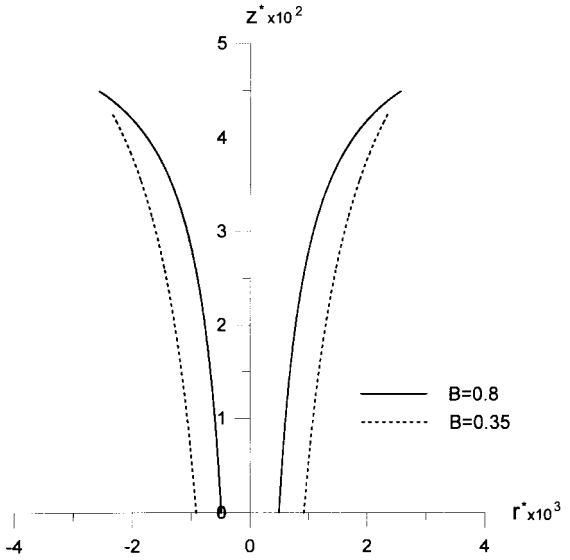


Fig. 8. Shapes of a pore for different values of dimensionless parameter governing decaying rate of displacement of solidification front ($A = 0.045$, $Bo = 10^3$, $m = 0.01$, $K^* = 10$, $C^*_\infty = 12$, $h^*_{\text{eff}} = 14$, $\phi = 4\pi/9$).

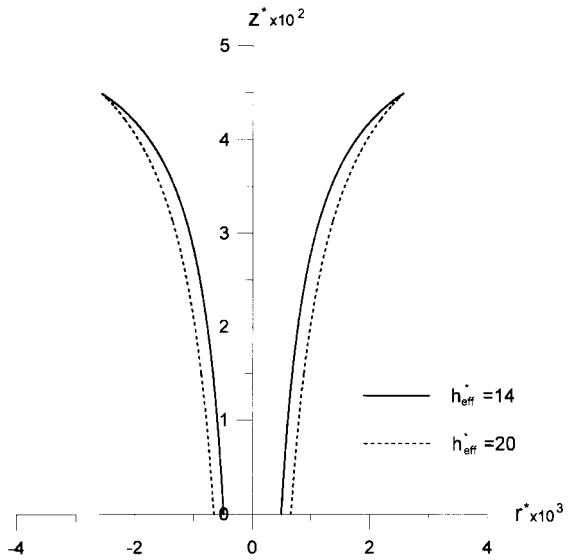


Fig. 10. Shapes of a pore for different values of dimensionless parameter governing steady component of mass transfer coefficient ($A = 0.045$, $B = 0.8$, $Bo = 10^3$, $m = 0.01$, $K^* = 10$, $C^*_\infty = 12$, $\phi = 4\pi/9$).

shape of the pore becomes narrow by decreasing the dimensionless parameter governing steady component of the mass transfer coefficient, as shown in Fig. 10. In Fig. 11, it shows that at a given time, an increase in the dimensionless parameter governing unsteady component of the mass transfer coefficient decreases the mass transfer coefficient which increases gas pressure in the pore. A smaller dimensionless parameter govern-

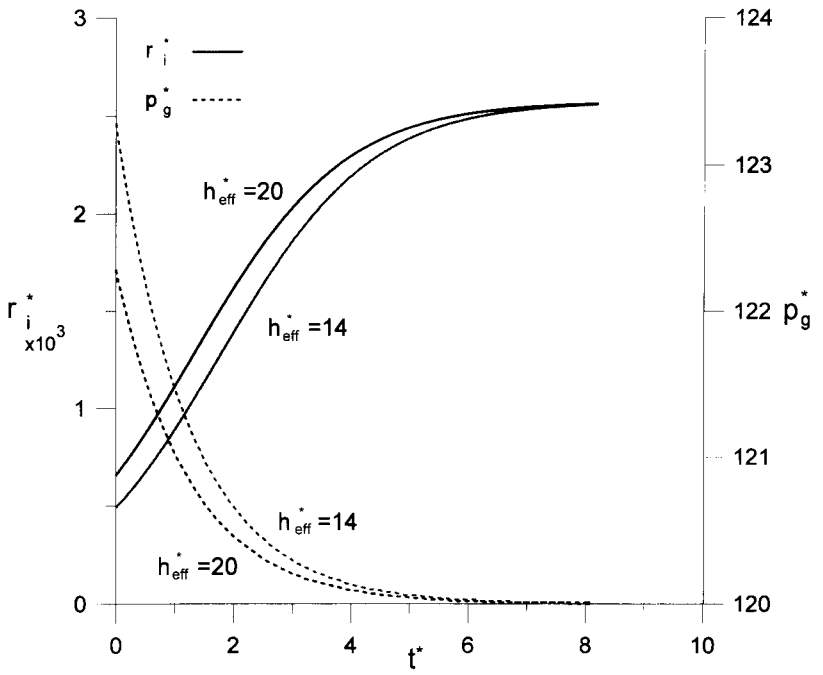


Fig. 9. Dimensionless cap radius and gas pressure in pore vs dimensionless time for different values of dimensionless parameter governing steady component of mass transfer coefficient ($A = 0.045$, $B = 0.8$, $Bo = 10^3$, $m = 0.01$, $K^* = 10$, $C^*_\infty = 12$, $\phi = 4\pi/9$).

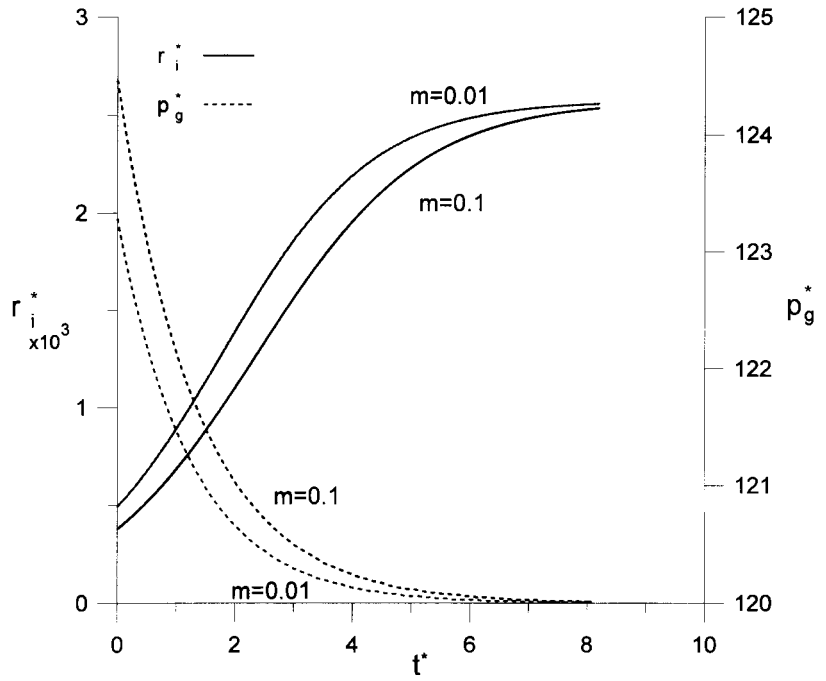


Fig. 11. Dimensionless cap radius and gas pressure in pore vs dimensionless time for different values of dimensionless parameter governing unsteady component of mass transfer coefficient ($A = 0.045$, $B = 0.8$, $m = 0.01$, $Bo = 10^3$, $K^* = 10$, $C^*_\infty = 12$, $h^*_{\text{eff}} = 14$, $\phi = 4\pi/9$).

ing unsteady component of the mass transfer coefficient produces a wider shape of the pore, as shown in Fig. 12.

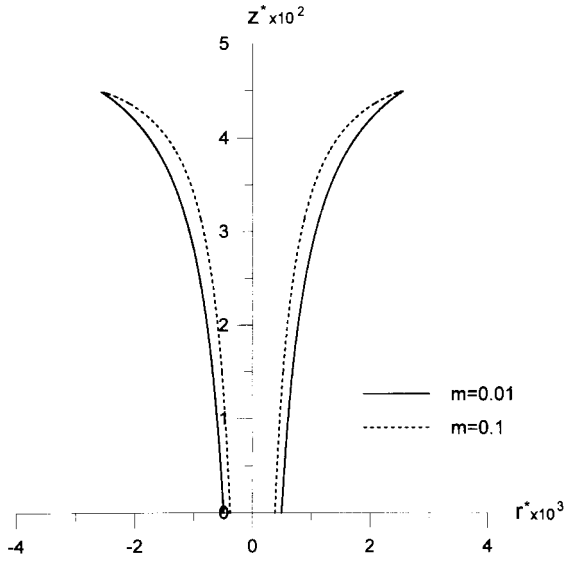


Fig. 12. Shapes of a pore for different values of dimensionless parameter governing unsteady component of mass transfer coefficient ($A = 0.045$, $B = 0.8$, $m = 0.01$, $Bo = 10^3$, $K^* = 10$, $C^*_\infty = 12$, $h^*_{\text{eff}} = 14$, $\phi = 4\pi/9$).

A slight increase in the modified dimensionless Henry's constant significantly increases dimensionless gas pressure and decreases cap radius, as shown in Fig. 13. An increase in the dimensionless Henry's constant indicates an increase in dimensionless gas pressure in order to maintain physico-chemical equilibrium and solute accumulation at the cap surface. The shape of the pore becomes narrow by increasing the dimensionless Henry's constant, as shown in Fig. 14. Fig. 15 shows that dimensionless gas pressure is decreased with dimensionless concentration in bulk liquid far from the solidification front due to decreases in gas solute at cap surface and mass transfer to the pore. A narrow pore induced by an increased dimensionless concentration in the bulk liquid is presented in Fig. 16.

As shown in Fig. 17, an increase in dimensionless parameter governing surface tension and cap angle increases dimensionless cap radius in order to satisfy momentum balance at cap surface. Interestingly, dimensionless gas pressure is found to be independent of the dimensionless parameter governing surface tension and cap angle. Axisymmetric shapes of the pore for different values of the dimensionless parameter governing surface tension and cap angle are shown in Fig. 18. A small dimensionless parameter governing surface tension and cap angle induces a narrow pore.

The measured displacement of the solidification front versus time in freezing water from Wei et al. [15]

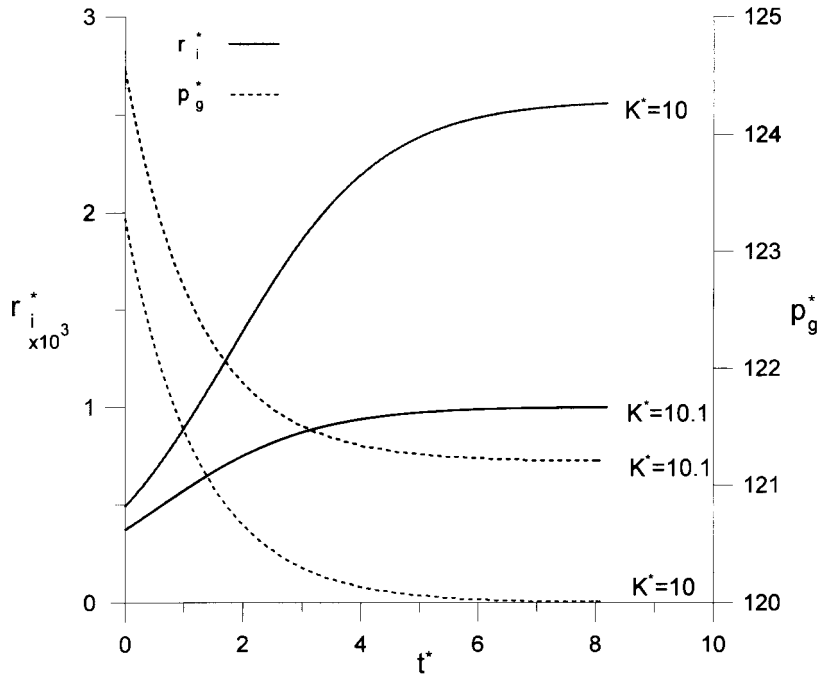


Fig. 13. Dimensionless cap radius and gas pressure in pore vs dimensionless time for different modified dimensionless Henry's constants ($A = 0.045$, $B = 0.8$, $Bo = 10^3$, $m = 0.01$, $C^*_\infty = 12$, $h^*_{\text{eff}} = 14$, $\phi = 4\pi/9$).

is shown in Fig. 19. The temperature at the bottom is $-18°C$, while that at the top is a surrounding temperature of 25°C. It can be seen that displacement of the advancing interface is of the order of $10^{-3}$ m. The maximum solidification rate is roughly $10^{-6}$ m/s in the early stage. Solidification rate decreases with increasing time and decreases to zero after time is greater than 4500 s. Choosing relevant values of dimensionless parameters $A = 0.0449$ and $B = 0.35$ governing the maximum displacement of the solidification front and decaying rate of displacement, respectively, it is found that Eq. (19) slightly overestimates and underestimates the measured displacement of the solidification front for times less and greater than 4500 s, respectively. In order to satisfy negligible displacement as time becomes large, dimensionless parameter $B = 0.8$ is chosen. The predicted displacement, however, is overestimated in earlier times.

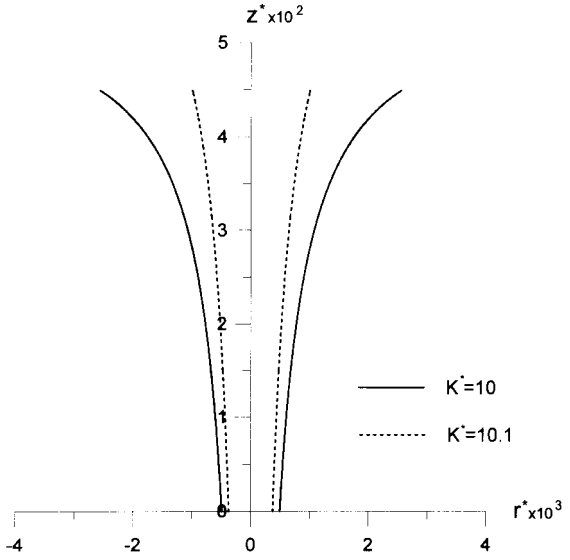


Fig. 14. Shapes of a pore for different modified dimensionless Henry's constants ($A = 0.045$, $B = 0.8$, $Bo = 10^3$, $m = 0.01$, $C^*_\infty = 12$, $h^*_{\text{eff}} = 14$, $\phi = 4\pi/9$).

The variation in the measured cap diameter with time is shown in Fig. 20 [15]. Evidently, cap diameter increases with time. Cap diameters are of the order of $10^{-4}$ m with the maximum growing rates of around $10^{-7}$ m/s in the earlier stage. It is found that the dimensionless parameter $B = 0.35$ cannot agree well with the unsteady variation in cap diameter. The increasing rate for cap diameter is less in earlier times and greater in later times than experimental data. Better results can be seen for the dimensionless parameter $B = 0.8$. Referring to Figs. 19 and 20, it implies that in view of an incomplete insulation of the glass tube during a long freezing time, the prediction based on one-dimensional analysis cannot fit well in

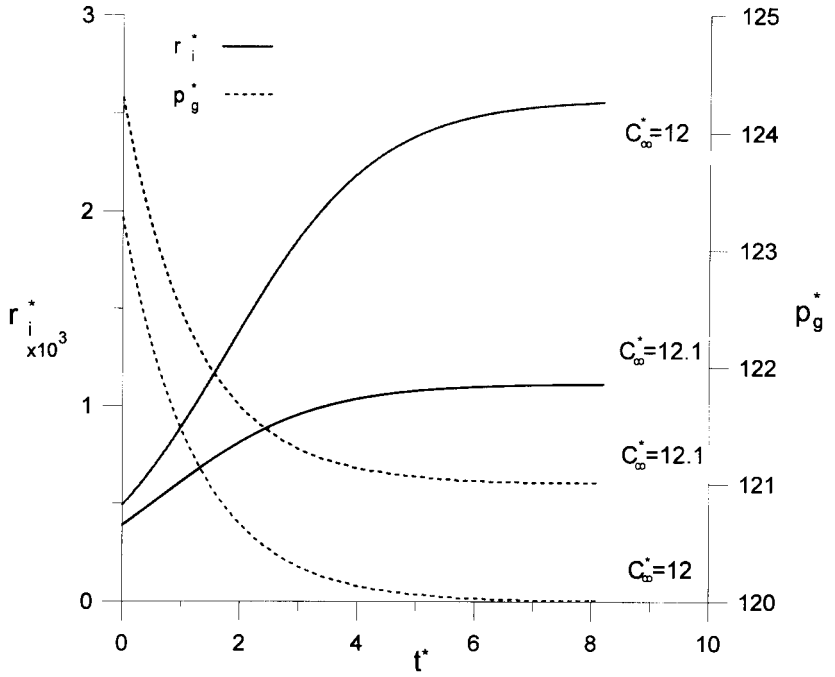


Fig. 15. Dimensionless cap radius and gas pressure in pore vs dimensionless time for different dimensionless concentrations in bulk liquid far from solidification front ($A = 0.045$, $B = 0.8$, $Bo = 10^3$, $m = 0.01$, $K^* = 10$, $h^*_{\text{eff}} = 14$, $\phi = 4\pi/9$).

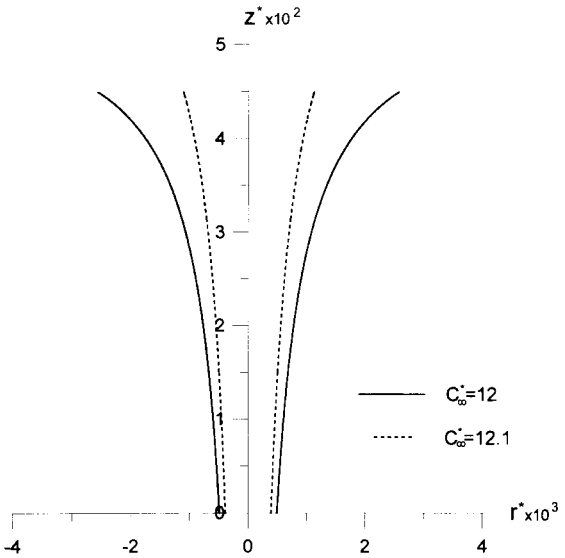


Fig. 16. Shapes of the pore for different dimensionless concentrations in bulk liquid far from solidification front ($A = 0.045$, $B = 0.8$, $Bo = 10^3$, $m = 0.01$, $K^* = 10$, $h^*_{\text{eff}} = 14$, $\phi = 4\pi/9$).

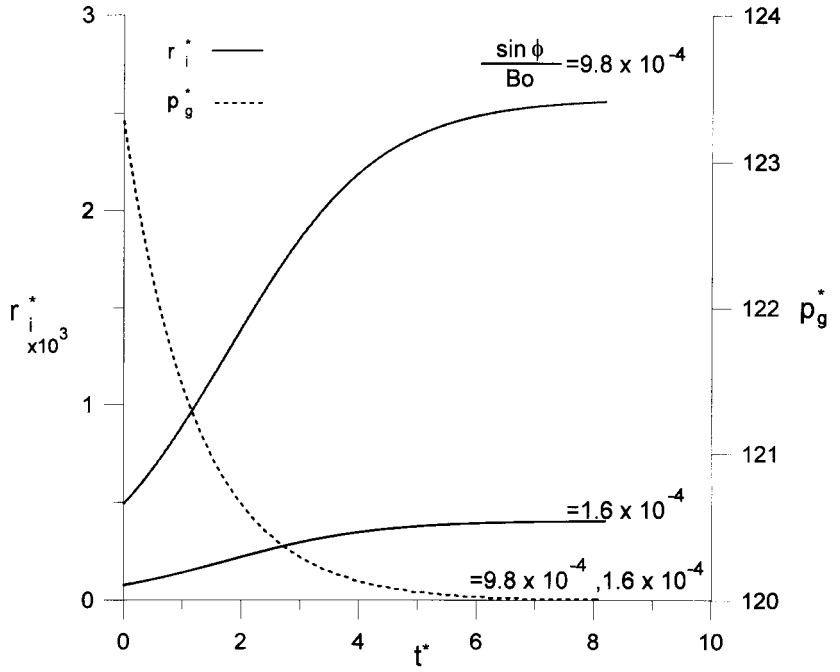


Fig. 17. Dimensionless cap radius and gas pressure in pore vs dimensionless time for different values of dimensionless parameter governing surface tension and cap angle ($A = 0.045$, $B = 0.8$, $Bo = 10^3$, $m = 0.01$, $K^* = 10$, $C_\infty^* = 12$, $h_{\text{eff}}^* = 14$).

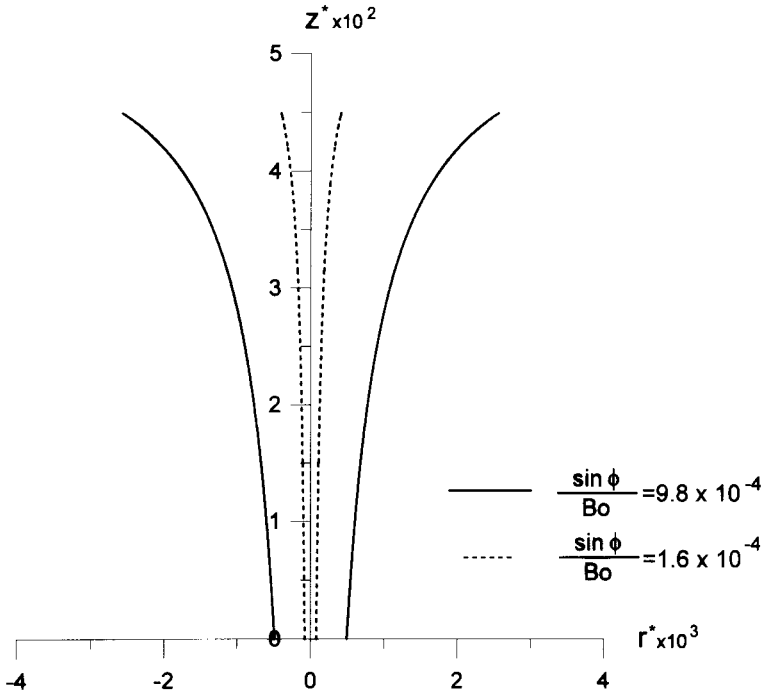


Fig. 18. Shapes of a pore for different values of dimensionless parameter governing surface tension and cap angle ($A = 0.045$, $B = 0.8$, $Bo = 10^3$, $m = 0.01$, $K^* = 10$, $C_\infty^* = 12$, $h_{\text{eff}}^* = 14$).

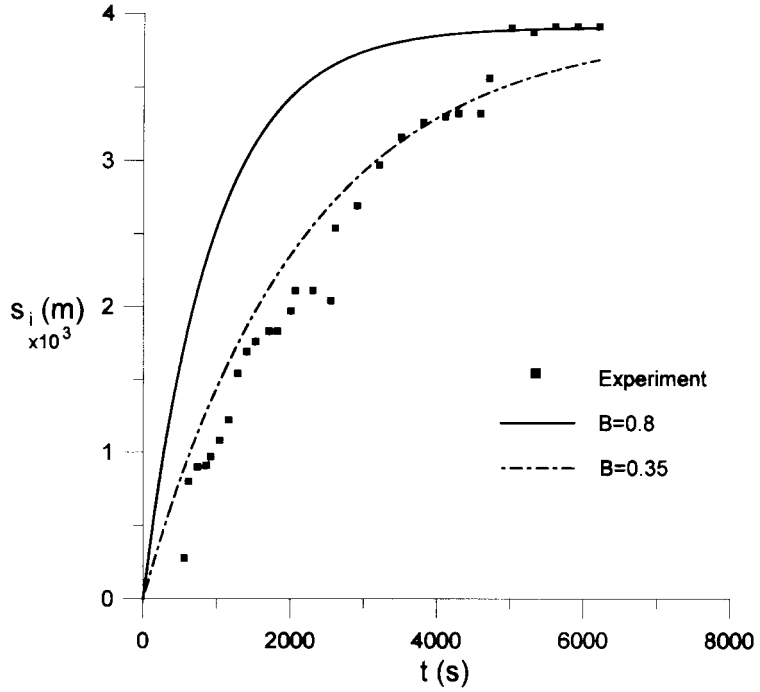


Fig. 19. Measured and predicted displacement of solidification front vs time ($A = 0.0449$, $h_{i0} = 0.087$ m, $D = 10^{-5}$ m$^2$/s).

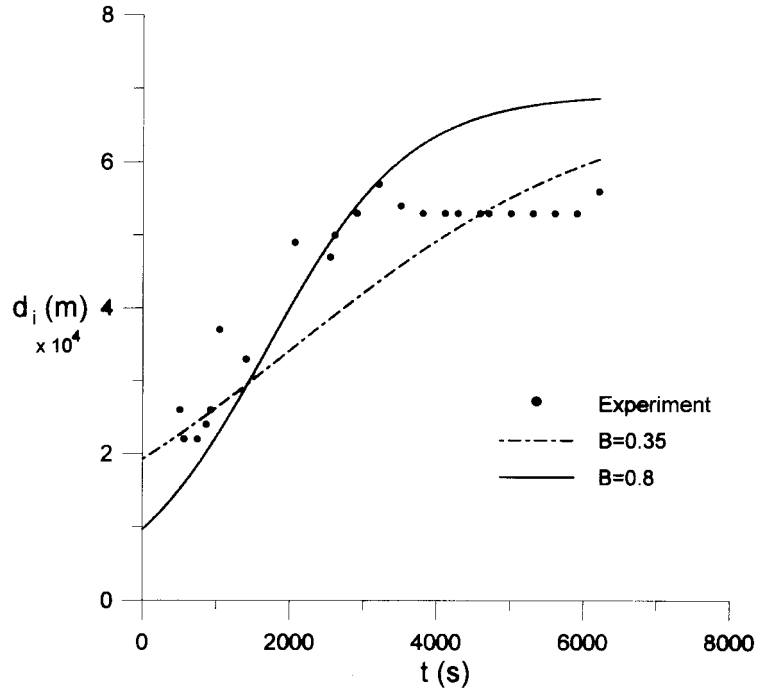


Fig. 20. Measured and predicted cap diameter vs time ($A = 0.0449$, $Bo = 10^3$, $m = 10^{-3}$, $K^* = 9.75$, $C^*_\infty = 12.28$, $h^*_{\text{eff}} = 14$, $\phi = 4\pi/9$, $h_{i0} = 0.087$ m, $D = 10^{-5}$ m$^2$/s).

the entire range of time. Eq. (19), however, is still acceptable for a clear and fundamental investigation on the growth of the pore.

## 5. Conclusions

The conclusions drawn are the following:

1. Photographic observation shows that the wall of a pore corrugates readily during solidification. Some pores in solid may disappear from rupture of the cap surface and entrapment of water. Pores in solid can also partially solidify during freezing owing to an existence of water in the pores.
2. The shape of a pore in a solid is strongly affected by solidification rate. Since gas in liquid highly accumulates at cap surface by increasing solidification rate, mass transport to the pore is enhanced and gas pressure in the pore is increased. A satisfaction of momentum balance leads to a decrease of cap radius. On the other hand, when the solidification rate decreases in the course of freezing, cap radius increases with time.
3. Radii of a pore in solid are reduced by decreasing dimensionless parameters governing steady component of the mass transfer coefficient, and surface tension and cap angle, and increasing dimensionless parameters governing the maximum displacement and decaying rate of displacement for the solidification front, Henry's constant, concentration in bulk liquid, and unsteady component of the mass transfer coefficient.
4. Gas pressure in the pore is insensitive to the variation in the dimensionless parameter governing surface tension and cap angle.

## Acknowledgements

The zoom microstereoscope was provided by Professor H. Y. Liu at the Department of Biological Sciences, National Sun Yat-Sen University.

## References

[1] J.D. Fast, in: Interaction of Metals and Gases, Academic Press, New York, 1965, pp. 112–120. Translated from Dutch by M.E. Mulder-Woolcock.
[2] J.A. Burton, R.C. Prim, W.P. Slichter, The distribution of solute in crystals grown from the melt. Part I. Theoretical, J. Chemical Physics 21 (1953) 1987–1991.
[3] W.A. Tiller, K.A. Jackson, J.W. Rutter, B. Chalmers, The redistribution of solute atoms during the solidification of metals, Acta Metallurgica 1 (1953) 428–437.
[4] D.T.J. Hurle, E. Jakeman, E.R. Pike, Striated solute distributions produced by temperature oscillations during crystal growth from the melt, J. Crystal Growth 3 (1968) 633–640.
[5] M.A. Bianchi, R. Viskanta, Gas segregation during solidification processes, International J. Heat and Mass Transfer 40 (1997) 2035–2043.
[6] N.E. Dorsey, in: Properties of Ordinary Water-Substance, Reinhold, New York, 1940, pp. 414–415.
[7] B. Chalmers, How water freezes, Scientific American 200 (1959) 114–122.
[8] A.E. Carte, Air bubbles in ice, Proceedings Physical Society London 77 (1961) 757–768.
[9] W.R. Wilcox, V.H.S. Kuo, Gas bubble nucleation during crystallization, J. Crystal Growth 19 (1973) 221–228.
[10] K.F. Vasconcellos, J. Beech, The development of blowholes in the ice/water/carbon dioxide system, J. Crystal Growth 28 (1975) 85–92.
[11] Ya.E Geguzin, A.S. Dzyuba, Gas evolution and the formation and capture of gas bubbles at the crystallization front when growing crystals from the melt, Soviet Physics, Crystallography 22 (1977) 197–199 (from Kristallografiya 22 (1977) 348–353).
[12] Ya.E Geguzin, A.S. Dzuba, Crystallization of a gas-saturated melt, J. Crystal Growth 52 (1981) 337–344.
[13] G. Lipp, Ch. Körber, S. Englich, U. Hartmann, G. Rau, Investigation of the behavior of dissolved gases during freezing, Cryobiology 24 (1987) 489–503.
[14] K. Tagavi, L.C. Chow, O. Solaiappan, Void formation in unidirectional solidification, Experimental Heat Transfer 3 (1990) 239–255.
[15] P.S. Wei, Y.K. Kuo, S.H. Chiu, The growth of a pore trapped in solid during solidification—experimental observation and theoretical modeling. Submitted to ASME J. Heat Transfer (1999).
[16] Oxygen and ozone-solubility data series. In: R. Battino (Ed.), International Union of Pure and Applied Chemistry, vol. 7, Pergamon Press, Oxford, 1981, pp. 1–40.
[17] Nitrogen and air-solubility data series. In: R. Battino (Ed.), International Union of Pure and Applied Chemistry, vol. 10, Pergamon Press, Oxford, 1982, pp. 1–29.
[18] S.M. Walas, Phase Equilibria in Chemical Engineering, Butterworth, Boston, 1985, p. 329.
[19] J.T. Davies, E.K. Rideal, Interfacial Phenomena, 2nd ed., Academic Press, New York, 1963 (Chapter 7).
[20] W.H. Giedt Chapter 18, Thermophysics, Van Nostrand Reinhold, New York, 1971, pp. 387–391.
[21] W.K. Lewis, W.G. Whitman, Principles of gas absorption, Industrial and Engineering Chemistry 16 (1924) 1215–1220.
[22] R. Higbie, The rate of absorption of a pure gas into a still liquid during short periods of exposure, Trans. AIChE 31 (1935) 365–389.
[23] D. Papamantellos, K.W. Lange, K. Okohira, H. Schenck, A mathematical approach for the mass trans-

fer between liquid steel and an ascending bubble, Metallurgical Transactions 2 (1971) 3135–3144.

[24] G.H. Geiger, D.R. Poirier, Transport Phenomena in Metallurgy, Addison-Wesley, Reading, MA, 1973, pp. 463–468.

[25] Nitrogen and air-solubility data series. In: R. Battino (Ed.), International Union of Pure and Applied Chemistry, vol. 10, Pergamon Press, Oxford, 1982, pp. 509–550.